

Powder diffraction in Bragg–Brentano geometry with straight linear detectors

Dominik Kriegner,^{a,*} Zdeněk Matěj,^{a,b} Radomír Kužel^a and Václav Holý^a

Received 20 January 2015

Accepted 18 February 2015

^aDepartment of Condensed Matter Physics, Charles University in Prague, Ke Karlovu 5, 121 16 Prague 2, Czech Republic, and ^bMax IV Laboratory, Lund University, Ole Rømers väg 1, 223 63 Lund, Sweden. Correspondence e-mail: dominik.kriegner@gmail.com

A common way of speeding up powder diffraction measurements is the use of one- or two-dimensional detectors. This usually goes hand in hand with worse resolution and asymmetric peak profiles. In this work the influence of a straight linear detector on the resolution function in the Bragg–Brentano focusing geometry is discussed. Because of the straight nature of most modern detectors geometrical defocusing occurs, which heavily influences the line shape of diffraction lines at low angles. An easy approach to limit the resolution-degrading effects is presented. The presented algorithm selects an adaptive range of channels of the linear detector at low angles, resulting in increased resolution. At higher angles the whole linear detector is used and the data collection remains fast. Using this algorithm a well behaved resolution function is obtained in the full angular range, whereas using the full linear detector the resolution function varies within one pattern, which hinders line-shape and Rietveld analysis.

1. Introduction

Powder diffraction is one of the most important material characterization methods. It enables determination of the crystalline nature of materials and thereby often chemical compositions, particle size and the nature of defects can be investigated (Klug & Alexander, 1974; Mittemeijer & Scardi, 2004; Dinnebier & Billinge, 2008; Guinebretière, 2013). The use of X-ray photons, because of their high penetration depth into matter, also allows one to combine powder diffraction methods with several sample environments, e.g. pressure cells, ovens, cryostats or chemical reaction cells. For such detailed investigations one needs fast recording of high-quality powder diffraction data in order to enable *in situ* investigation. At synchrotron sources this is possible with sub-second integration times using two-dimensional detectors (He, 2009; Liermann *et al.*, 2010). However, using laboratory sources, because of much lower intensities, a few minutes are needed to obtain a powder diffraction pattern of decent quality. In comparison to measurements with a point detector, the decrease of the acquisition time using linear and area detectors in the laboratory is still dramatic (Göbel, 1979; Reiss, 2002). Usually, however, this has the drawback of reduced resolution and higher background due to a lack of collimation (Cheary & Coelho, 1994; Słowik & Zięba, 2001; Guinebretière *et al.*, 2005). Modern one-dimensional solid-state detectors [MYTHEN (Schmitt *et al.*, 2003; Bergamaschi *et al.*, 2008), PIXcel (Reiss, 2002; Wright *et al.*, 2004), Bruker LYNXEYE (Bruker Corporation, 2015)] with low cross-talk can be considered as an array of point detectors. Therefore the achievable speed-up is comparable to the number of available channels, which can easily be of the order of 1000.

Most dedicated laboratory powder diffraction instruments work in a variation of the Bragg–Brentano focusing geometry. This allows the use of a divergent X-ray beam from a sealed tube without monochromatization or parallelization and therefore avoids the big loss of intensity connected with such a beam preparation. The most common

goniometer geometries are the so-called Bragg–Brentano θ – θ geometry with a fixed sample or θ – 2θ geometry with a fixed X-ray tube (Mittemeijer & Welzel, 2013). In these geometries the detector and source are located at the intersection points of the goniometer circle (fixed radius) and the focusing circle, whose radius varies with the goniometer angle. The sample is placed tangentially to the focusing circle in the centre of the goniometer. The resolution function of such instruments when using point detectors has been discussed extensively in the literature (see Guinebretière *et al.*, 2005, and references therein). A straight detector mounted perpendicularly to the detector arm is not the best solution in either of the two Bragg–Brentano geometries since it is not positioned tangentially to the focusing circle. Fig. 1(a) illustrates this effect for low and high goniometer angles θ , whereas Fig. 1(b) shows the large impact on the powder diffraction lines at low angles. Other geometries, like the Seemann Bohlin geometry (Klug & Alexander, 1974; Guinebretière *et al.*, 2005), where the sample is not located in the centre of rotation of the detector circle, overcome this problem since the focusing circle has a constant radius; however, they are mechanically more elaborate to set up and therefore seldom used. The problem is further exacerbated by the rather low goniometer radii of laboratory diffractometers, which typically are only around 20–30 cm. Using larger goniometer radii the problem is relatively smaller, but owing to the smaller angular coverage of the detector the data acquisition is also decreased.

The resolution function obtained when using linear detectors was discussed previously (Cheary & Coelho, 1994; Słowik & Zięba, 2001); however, standard powder diffraction software cannot account for these effects. To allow a standard analysis the effect of defocusing, resulting from the use of a linear detector, has to be limited; otherwise strong asymmetries and peak broadening, as shown in the work by Paszkowicz (2005) and clearly visible in Fig. 1(b), destroy the resolution function at low angles. Previously, only a constant limita-

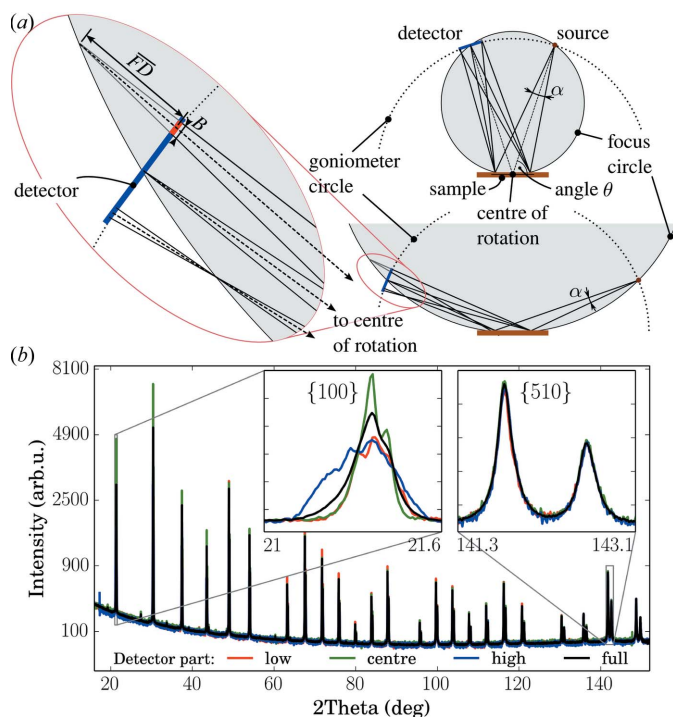


Figure 1
 (a) Sketch of the defocusing due to a straight linear detector used in Bragg–Brentano geometry. At lower angles, where the focusing circle is large and the orientation of the detector is very unfavourable, large blurring of the signal results from the use of the linear detector. (b) shows the powder diffraction pattern of a LaB_6 powder obtained using different parts of the linear detector. Insets show the line shape of the {100} and {510} peaks; double peaks arise from the $\text{Cu } K\alpha_{1,2}$ doublet.

tion of the angular width of the detector was suggested (Reiss, 2002). In this report we present a way to properly integrate a straight linear detector into the Bragg–Brentano geometry, while maintaining a well defined resolution function in the full angular range. Our idea is based on limiting the geometrical defocusing at low angles by using only part of the linear detector as suggested by Słowik & Zięba (2001) and earlier by Cheary & Coelho (1994); however, no rules were given as to how such a limitation should be achieved. At higher angles, where the geometrical defocusing is small, the full detector is used and considerable speed-ups are maintained. Data obtained using this approach can be analysed with standard Rietveld software (Rodríguez-Carvajal, 1993; Lutterotti *et al.*, 1999; Larson & Von Dreele, 2000; Matěj *et al.*, 2010; Coelho *et al.*, 2011). The structure of this paper is as follows: after introducing the theoretical foundations of our considerations, we show how our approach influences the line shape of a NIST reference material for powder diffraction. At the end we discuss how a well defined line shape in a large angular range can be obtained using the presented algorithm.

2. Theoretical foundations

Using a straight linear detector in a powder diffraction measurement enables the simultaneous acquisition of the signal diffracted at different scattering angles 2θ . When used during a θ – θ or θ – 2θ scan with the respective goniometer at every goniometer angle the full detector spectrum is acquired, resulting in the collection of a two-dimensional data set. These two-dimensional data are then reduced to a one-dimensional powder diffraction pattern. For this we ascribe

every channel n of the *straight* linear detector, located at a distance d from the detector centre, a certain 2θ angle. We define d as

$$d = (n - n_0)w, \quad (1)$$

with n_0 the centre channel hit by the centre of the primary beam at zero angle and w the width of one pixel of the detector. The resulting scattering angle for any detector pixel is then

$$2\theta(n) = 2\theta_{\text{CCH}} + \arcsin\left(\frac{d(n)}{L} \frac{\cos \beta}{\{1 + [(d(n)/L]^2 - 2[d(n)/L] \sin \beta\}^{1/2}}\right), \quad (2)$$

where $2\theta_{\text{CCH}}$ is the angular position of the channel n_0 and L is the distance of the detector from the centre of rotation. The angle β accounts for small misalignments/detector tilts, considering situations when the detector is not mounted perpendicular to the ray hitting the centre channel. Using the algorithms presented in the work by Kriegner *et al.* (2013) these misalignments can be determined and aligned to be zero. In our further discussion we therefore set $\beta = 0$.

After a scattering angle has been assigned to every channel the data can be binned to a regular grid of 2θ values. During this process for each 2θ value the corresponding data are summed. Details about the applied binning algorithm can be found in Appendix A. However, because of the defocusing at the channels far away from the centre channel, the signal shape on different parts of the detector varies. In Fig. 1(b) we show the signal obtained from (i) the full one-dimensional detector, (ii) only the central 5 mm of the detector, (iii) the lower 5 mm of the detector, (iv) the upper 5 mm of the detector.

The data were obtained from a LaB_6 powder [NIST 660b (National Institute of Standards & Technology, 2010)] using a 64 mm-wide straight detector (MYTHEN 1K) with 1280 channels (each $50 \mu\text{m}$) and Cu radiation. We used a refurbished Siemens D500 goniometer with a source–sample and sample–detector distance of 330 mm. The measurement was performed in reflection geometry with a fixed divergence slit size, resulting in a primary beam with 0.44° divergence. The detector window was covered by an Ni foil in order to suppress the $\text{Cu } K\beta$ line. Clearly the data from the edges of the detector [(iii) and (iv)] are heavily affected by the defocusing, leading to a disastrous line shape at low-angle peaks. Using the signal from the whole detector to produce the powder diffraction pattern (i) one obtains a slightly asymmetric line shape which hardly allows the $\text{Cu } K\alpha_{1,2}$ doublet to be resolved, whereas when using only the central 5 mm (ii) the line shape is more symmetric and the $\alpha_{1,2}$ doublet is more pronounced. At higher-angle peaks the effects of the defocusing are negligible, leading to the same line shape for all the signals. At lower angles one should also consider that the footprint is significantly different for signals recorded on either side of the detector since the measurement was performed with a fixed slit system. The deviations induced by the parafocusing geometry (flat sample), leading to a broadening and shift of the peaks, cause a smearing of the signal when the collected data are reduced to the one-dimensional powder pattern. This smearing caused by the flat sample is one of the reasons why the signal from the upper part of the detector (blue curve in Fig. 1b), which records the {100} line at lower goniometer angles, is more broadened than the signal from the lower end of the detector (red curve in Fig. 1b) recorded at higher goniometer angles. Of course, not only the smearing due to the parafocusing but also the defocusing and blurring due to the linear detector increase at smaller goniometer angles. This is another reason for the wide signal of the upper part of the detector. Note that in the Bragg–Brentano geometry even a curved detector would not solve the problem since

the radius of the focusing circle depends on the goniometer angle (see Fig. 1*a*). A detector with constant curvature [e.g. the MYTHEN 24K or similar systems (Dectris, 2014)] is very well suited for a parallel beam setup or for the Seemann Bohlin geometry, but does not allow the use of a divergent beam as present in the standard Bragg–Brentano geometry when scanning the goniometer angle.

In order to obtain a proper line shape for the full angular range, we consider how the defocusing length (\overline{FD} in Fig. 1*a*) changes with the goniometer angle θ and varies for different positions on the detector. From geometrical considerations it follows that the defocusing \overline{FD} is

$$\overline{FD}(\theta, d) = \frac{d}{[1 + (d/L)^2]^{1/2}} \cotan \theta. \quad (3)$$

We further define the more relevant blurring width B , which specifies the width into which the scattered signal is blurred on the detector (Fig. 1*a*). B depends not only on the detector distance but also on the irradiated sample length S . For an irradiated sample length S small enough in comparison with the detector distance ($S/L \ll 1$) one obtains

$$B \simeq \left| \frac{\overline{FD} S \sin \theta}{\overline{FD} + (L^2 + d^2)^{1/2}} \right|. \quad (4)$$

This means that the blurring is different in the case of fixed or variable slits, which results in either variable or constant S , respectively. If one works with fixed slits, resulting in a change of the irradiated sample length with the goniometer angle, one has to consider that S depends on θ as

$$S = \begin{cases} S_0 & \text{if } L\alpha/\sin \theta > S_0, \\ L\alpha/\sin \theta & \text{otherwise.} \end{cases} \quad (5)$$

Here we use the beam footprint on the sample as approximated in the work by Słowik & Zięba (2001), which uses the primary beam divergence α (indicated in Fig. 1*a*). The size of the sample S_0 is used to limit the maximum illuminated length at low angles. Fig. 2 shows

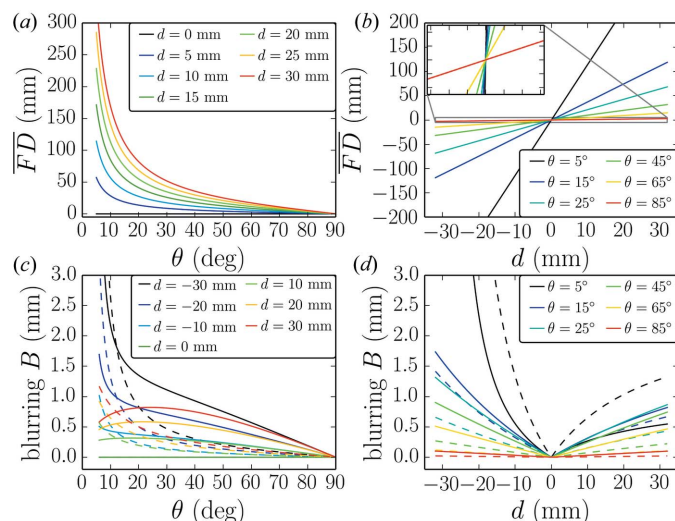


Figure 2

Defocusing length \overline{FD} and blurring B versus goniometer angle θ and distance from the detector centre d . (a) shows the angular dependence of the defocusing length for several positions on the detector. (b) shows the variation of \overline{FD} on the detector for fixed goniometer position. The inset shows a zoom to the high-angle curve. (c) shows the angular dependence of the blurring, while (d) shows the variation of B along the detector for certain fixed angles. (c) and (d) are shown for variable slits (full lines) and fixed slits (dashed lines). The parameters used for the calculations are $L = 330$ mm, $\alpha = 0.44^\circ$ and $S_0 = \infty$ for the fixed-slit case and $S = 12$ mm in the case of variable slits.

how the defocusing length and the blurring vary with the goniometer angle and position on the detector. The defocusing length rapidly increases at low goniometer angles as expected and changes approximately linearly for different positions on the detector as suggested by equation (3). The blurring, however, has a more elaborate dependence on the goniometer angle in the case of a variable-slit system (full lines in Figs. 2*c* and 2*d*). For the upper part of the detector it decreases at low angles owing to the small projected size of the sample, while it diverges for the lower parts of the detector. This divergence is due to the fact that parts of the detector reach below the sample horizon and therefore the defocusing length is ill defined. In the case of a fixed-slit system (dashed lines in Figs. 2*c* and 2*d*) the blurring has a similar angular dependence to the defocusing length.

In order to obtain a better resolution function we shall now limit resolution-degrading effects by limiting the blurring. By inverting the expression in equation (4) we find which parts of the detector should be used in order to obtain a powder diffraction pattern that is only weakly affected by resolution degrading due to the linear detector. We need to differentiate between the upper and lower sides of the detector. The usable detector parts, which yield a blurring smaller than B , are between d_{\min} and d_{\max} , for which we find the following analytic expressions:

$$d_{\min} = -\frac{L}{2} \left(1 + \frac{S}{B} \sin \theta \right) \cotan \theta + \left\{ \left[\frac{L}{2} \left(1 + \frac{S}{B} \sin \theta \right) \cotan \theta \right]^2 + L^2 \right\}^{1/2} \quad (6)$$

and

$$d_{\max} = -\frac{L}{2} \left(1 - \frac{S}{B} \sin \theta \right) \cotan \theta - \left\{ \left[\frac{L}{2} \left(1 - \frac{S}{B} \sin \theta \right) \cotan \theta \right]^2 + L^2 \right\}^{1/2}. \quad (7)$$

The result of the inversion depicting both d_{\min} and d_{\max} is shown in Fig. 3 for the case of a fixed-slit [S from equation (5)] and a variable-

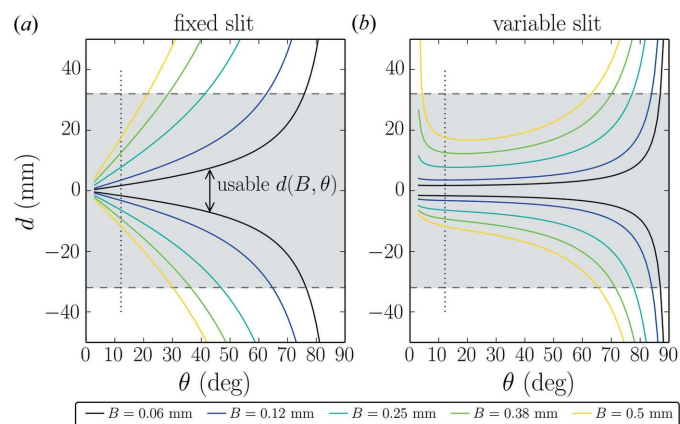


Figure 3

Usable detector width in order to limit the effect of blurring. (a) shows the usable detector offsets d_{\min} and d_{\max} from equations (6) and (7) for a given length of B for a fixed slit [S from equation (5)], where the area between the curves of the same colour gives the range of d values to be used. (b) shows the same, but as deduced for variable slits. Dashed lines indicate the extension of our detector. A dotted line marks the position where the irradiated sample lengths are equal for both slit settings. The parameters used were $L = 330$ mm, $\alpha = 0.44^\circ$ and $S_0 = \infty$ for the fixed-slit case and $S = 12$ mm in the case of variable slits.

slit system (fixed S). In both cases this dictates the use of only the central part of the detector at low angles, as intuitively expected and previously suggested (Cheary & Coelho, 1994; Słowik & Zięba, 2001). The variable- and fixed-slit cases cannot easily be compared since in the variable-slit case the chosen irradiated sample length influences the result. At the goniometer angle θ , at which the fixed slit and variable slit yield an equal irradiation sample length (marked by a vertical dotted line in Fig. 3), the two cases are of course equal. Note that an attempt to limit the blurring of the signal to the width of only one detector channel (50 μm in our setup) allows the use of only the central millimetres of the detector even at higher goniometer angles and therefore makes the linear detector mostly useless. For the present geometry it is therefore an illusion to reach the resolution given by the channel width of the linear detector. Using the linear detector one has to accept a certain blurring of the signal in order to obtain an accelerated data acquisition.

3. Results

With the same setup as used for the data shown in Fig. 1 we measured a powder diffraction pattern from LaB_6 . Using the limited detector width as shown in Fig. 3(a) we extracted several powder diffraction patterns from a θ - θ scan. Because of the adaptive number of channels, at every angular position a different number of channels contributes to the signal; therefore a normalization is needed during the binning algorithm. For this purpose we use the number of channels contributing to every data bin. The statistical error of the data is calculated from the raw intensities before the normalization. Fig. 4 shows a close-up of the $\{100\}$ peak in comparison with the signal obtained from only the central five channels and the signal using the data from all detector channels. An example of a full pattern is shown in Fig. 5(b). A clear broadening of the low-angle peaks is observed when higher blurring or all channels are used. The full width at half-maximum (FWHM) of the low-angle powder diffraction peaks is also clearly affected when more blurring is accepted (Fig. 4b). This is in contrast to the higher-angle peaks such as the $\{510\}$ line of LaB_6 at $2\theta > 140^\circ$. In addition to the FWHM, the peak shape of the lower-

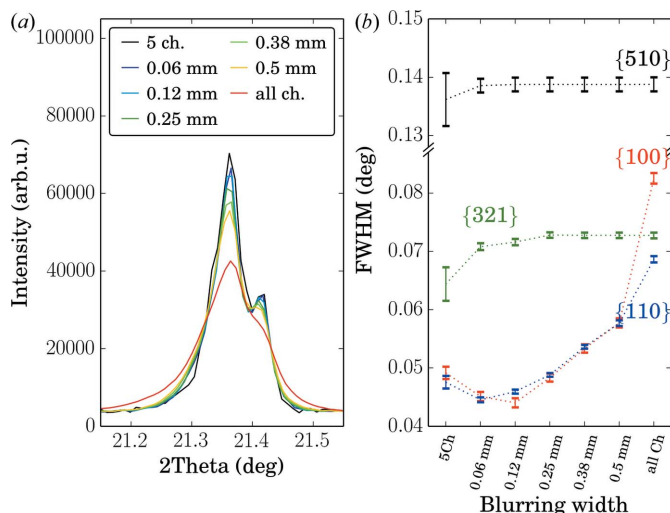


Figure 4 (a) Influence of different blurring width on the peak shape of the $\{100\}$ peak of an LaB_6 powder. Also shown is the obtained peak shape when only the five central or all detector channels are used. A clear broadening is observed when higher blurring is tolerated, i.e. more detector channels contribute to the shown signal. The intensity has been rescaled to the same background level between the Bragg peaks. In (b) the influence on the FWHM of several powder lines is shown.

angle peaks is modified by the blurring. More blurring leads to more pronounced tails of the powder diffraction lines.

Rietveld refinement (Rietveld, 1969) and whole powder pattern modelling (Ribárik *et al.*, 2001; Scardi & Leoni, 2002) are nowadays the most common approaches in powder diffraction data analysis of crystalline materials. An important component of these methods is a description of the diffraction profile width and shape. Software such as *Topas* (Coelho *et al.*, 2011) or *Jana* (Petříček *et al.*, 2014), based on a fundamental approach (Cheary & Coelho, 1992), can make use of the appropriate instrumental functions for straight linear detectors as described in the literature (Cheary & Coelho, 1994; Słowik & Zięba, 2001) and can in principle face the problem properly without any additional instrumental precautions. Other programs such as e.g. *Fullprof* (Rodríguez-Carvajal, 1993), *Maud* (Lutterotti *et al.*, 1999), *GSAS* (Larson & Von Dreele, 2000), *PM2K* (Leoni *et al.*, 2006) or *MStruct* (Materěj *et al.*, 2014) use phenomenological peak functions, e.g. pseudo-Voigt or Pearson VII (Young & Wiles, 1982), with angular dependence of profile parameters (FWHM, shape parameter and asymmetry) described by polynomial functions. This approach was originally designed for neutrons (Caglioti *et al.*, 1958); however, it is also extensively used for X-ray and synchrotron powder diffraction (Louër & Langford, 1988; Langford & Louër, 1996; McCusker *et al.*, 1999). Within this approach the angular dependence of the profile parameters has to be described by polynomial interpolation functions. In particular the angular dependence of the squared FWHM_p

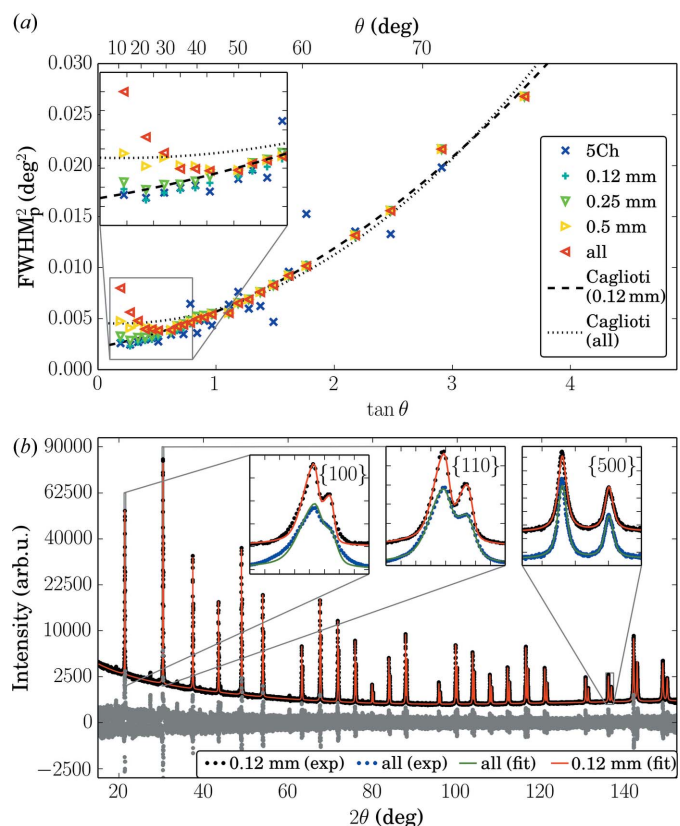


Figure 5 (a) FWHM of all peaks plotted *versus* $\tan \theta$ for different values of accepted blurring (Caglioti plot). The inset shows the deviation from the usual behaviour at low angles when more parts of the detector are used. (b) Rietveld analysis of the powder diffraction pattern extracted with 0.12 mm allowed blurring. Shown are the experimental data together with the fit and their difference on a square-root scale. The insets show a comparison of fits for 0.12 mm allowed blurring or when all channels are used for the $\{100\}$, $\{110\}$ and $\{500\}$ Bragg peaks. The curves are vertically shifted for clarity.

Table 1

The weighted-profile R value, R_{wp} , the statistically expected R value, R_{exp} , and their ratio, χ^2 , for data with different allowed blurring.

A typical diffraction pattern had approximately 20 000 points and 43 parameters were refined with one constraint.

	R_{wp} (%)	R_{exp} (%)	χ^2
All	4.63	2.12	2.18
Blur 0.5 mm	4.26	2.45	1.74
Blur 0.38 mm	3.98	2.62	1.52
Blur 0.25 mm	4.04	2.91	1.39
Blur 0.12 mm	4.42	3.62	1.22
Five channels	27.1	31.1	0.873

parameter should be precisely interpolated by the second-order Caglioti polynomial in $\tan \theta$ with three independent parameters U , V and W :

$$\text{FWHM}_p^2 = U \tan^2 \theta + V \tan \theta + W. \quad (8)$$

FWHM_p is a formal parameter used in the definition of the pseudo-Voigt function and does not include the correction for peak asymmetry. Fig. 5(a) shows the angular dependence of the FWHM_p parameter of asymmetric pseudo-Voigt profiles fitted to the measured data. Evidently there is an additional broadening at low angles in Fig. 5(a) when using all the detector channels or allowing a higher blurring. The dashed and the dotted lines show the fit of the data with 0.12 mm allowed blurring and for the case when all the detector channels are used, respectively. Only the former case can be accounted for using the Caglioti approach. This is also reflected in the attempt of a Rietveld refinement performed by *MStruct*, which is shown in Fig. 5(b). The broadened low-angle peaks integrated from all the detector channels can hardly be described using the common approach of resolution function determination (see deviation in insets). In Table 1 we list the weighted-profile R value R_{wp} , the expected R value R_{exp} and their ratio, the goodness of fit χ^2 (McCusker *et al.*, 1999), for Rietveld refinements of data with different allowed blurring. Increased blurring results in a worse goodness of fit. On the other hand limiting the blurring discards data from edge channels, especially at low diffraction angles, and therefore decreases the statistical quality of the data. This is clearly visible in the R_{exp} value (Table 1). For the data integrated with the fixed detector slit (five channels) R_{exp} is very high and the data are practically unusable, whereas data with an allowed blurring width of 0.12 mm already have $R_{exp} < 5\%$, which is acceptable. The reduced counting statistics finally also limit the choice of the allowed blurring width for the particular acquisition time used. Limiting the blurring reduces the goodness of fit which indicates an improved fit result. However, using only the central five channels results in a goodness of fit $\chi^2 < 1$, proof of the insufficient counting statistics in this data set. A compromise has to be made between reduction of blurring and loss of counting statistics.

Different Rietveld software suites propose more or less parameters to describe the angular dependence of the profile function. The appropriate parameters used particularly in *MStruct* (Matěj *et al.*, 2010) are (i) the Caglioti polynomial [equation (8)] for FWHM_p ; (ii) a linear trend in θ for the angular dependence of the shape parameter (Lorentzian–Gaussian character); and (iii) a quadratic polynomial in $1/\sin \theta$ for the asymmetry of the diffraction peaks below a certain limiting angle ($2\theta_{\min} = 60^\circ$). Although for the demonstration we used *MStruct*, we note that a similar improvement of the fit was observed when using *Maud* (Lutterotti *et al.*, 1999). Despite these differences, all software packages have to face the problem of approximating the curved angular dependence of FWHM_p^2 at low incidence angles in the

unfavourable case of using all the detector channel as depicted in Fig. 5(a). Moreover Fig. 5(a) is plotted for the formal parameter FWHM_p and the effect is even enhanced by peak asymmetry if plotted with the corrected FWHM values. In addition to the profile parameters we fitted parameters describing the background, sample displacement and the intensity of all the diffraction lines.

The analysis presented in Fig. 5 shows that the blurring effects result in an obscured profile function at low diffraction angles when all the channels of a long straight linear detector are used. This is difficult to treat with most Rietveld software. By the introduction of a finite blurring width a recipe is given for data integration which gives well defined peak profiles even at low 2θ angles and improves the goodness of fit.

4. Discussion and conclusion

In order to apply the presented recipe one has to calculate equations (6) and (7) for a particular goniometer geometry to get the usable detector parts. Using the Caglioti plot as shown in Fig. 5(a) one selects the blurring that still gives a well defined angular dependence of the resolution function. In our case the limiting values of broadening are between $B = 0.12$ and 0.25 mm. For higher allowed blurring a clearly increased FWHM_p value is observed. The limiting value of blurring, which we determine from the Caglioti plot, if also recalculated to an angular value [$\arctan(B/L)$] corresponds to the narrowest peak width obtainable with our setup. This intrinsic width w_{in} , which can be achieved by a point detector with a very narrow slit, is determined by other instrumental effects, *e.g.* axial divergence, finite sample size and finite penetration depth, surface roughness, and intrinsic sample broadening. In our case it is close to $w_{in} = 0.045^\circ$ as seen in Fig. 5(a). From this we conclude that the most straightforward way to choose a particular useful value of B is to use the best obtainable peak width when using a small detector slit and use $B \simeq L \tan w_{in}$. For the presented data this yields $B = 0.25$ mm, in agreement with the more elaborate determination. The selected blurring width also has implications for the acquisition time. Lower blurring results in fewer channels contributing to the data and the count time should be accordingly increased. Once an optimal value of allowed blurring is found, it can be used to extract powder diffraction data from measurements with a straight one-dimensional detector as long as the same geometry is maintained. It is important to note, however, that there are some limitations to the use of an adaptive number of channels depending on the goniometer angle. The presented approach works perfectly fine in the case of weakly or untextured samples, where the change of the integration width with the goniometer angle can be accepted. For strongly textured samples this might be problematic since the data at different angles are constructed using data obtained with different ranges of incidence angle θ , which will affect their intensities. Our approach is significantly easier than modelling the blurring due to the linear detector as attempted previously (Cheary & Coelho, 1994; Słowik & Zięba, 2001). An alternative solution to minimize the blurring would be the rotation of the detector depending on the goniometer angle θ in such a way as to have the detector aligned tangentially to the focusing circle. This requires an additional motor and makes the use of flight tubes, suppressing air scattering, impractical. Moreover, the advantage with the rotation in comparison to our method is rather limited since the obtained angular coverage at low angles decreases heavily, and due to the non-perpendicular incidence of the X-ray beam the angular acceptance of the detectors starts to be important. Instead our solutions, which can be integrated in any data-acquisition soft-

ware, provide an easy way of improving the powder diffraction data quality when linear detectors are used in Bragg–Brentano geometry. They enable fast measurements while resulting in improved resolution especially at low angles. Because of the well behaved resolution function a better goodness of fit can be obtained in Rietveld analysis.

APPENDIX A

Fuzzy binning algorithm

To extract one-dimensional powder diffraction data from the two-dimensional data set obtained from a θ – θ scan with a linear detector, one has to map every data point to a 2θ value. Instead of a standard binning/histogram algorithm, which assigns every data point to only one output bin, we use an extended binning algorithm which assigns every data point a certain width and if within this width there are more output data bins this data point is spread over these bins according to its overlap. The fraction of the overlap with the bins is furthermore summed to be used for normalization purposes. Before the normalization we calculate the error due to the counting statistics from the summed raw data. This error can be given to the Rietveld software to correctly calculate the residuals. After the normalization it is no longer possible to extract the errors of the data since, due to the adaptive number of channels, the different parts of the pattern do not necessarily have the same counting statistics. Unfortunately most powder diffraction software cannot account for this additional error data column. We therefore rescale the data and errors with the average of the normalization array in order to arrive at data corresponding as close as possible to the raw signal. The width of every data point needed for the distribution over multiple bins is obtained from the angular width of one channel of the detector. Therefore this approach describes quite well the real situation of the data acquisition and is also known as fuzzy binning. An implementation of this algorithm can be found in *xrayutilities* (Kriegner *et al.*, 2013).

We thank P. Doležal (Charles University) for helpful discussions, H. Reichlová for careful reading of the manuscript and the Czech Science Foundation (project 14-08124S) for financial support. DK acknowledges the support of the Austrian Science Fund (FWF): J3523-N27.

References

Bergamaschi, A., Broennimann, C., Dinapoli, R., Eikenberry, E., Gozzo, F., Henrich, B., Kobas, M., Kraft, P., Patterson, B. & Schmitt, B. (2008). *Nucl. Instrum. Methods Phys. Res. Sect. A*, **591**, 163–166.
 Bruker Corporation (2015). Bruker LYNXEYE XE 1D Detector, <http://www.bruker.com>.
 Caglioti, G., Paoletti, A. & Ricci, F. P. (1958). *Nucl. Instrum.* **3**, 223–228.

Cheary, R. W. & Coelho, A. (1992). *J. Appl. Cryst.* **25**, 109–121.
 Cheary, R. W. & Coelho, A. (1994). *J. Appl. Cryst.* **27**, 673–681.
 Coelho, A. A., Evans, J., Evans, I., Kern, A. & Parsons, S. (2011). *Powder Diffr.* **26** (Suppl. S1), S22–S25.
 Dectris (2014). MYTHEN Detector System, https://www.dectris.com/mythen_configurations.html.
 Dinnebier, R. E. & Billinge, S. J. L. (2008). *Powder Diffraction: Theory and Practice*. Cambridge: Royal Society of Chemistry.
 Göbel, H. E. (1979). *Adv. X-ray Anal.* **22**, 255–265.
 Guinebretière, R. (2013). *X-ray Diffraction by Polycrystalline Materials*. London: Wiley-ISTE.
 Guinebretière, R., Boule, A., Masson, O. & Dauger, A. (2005). *Powder Diffr.* **20**, 294–305.
 He, B. B. (2009). *Two-Dimensional X-ray Diffraction*. New Jersey: Wiley.
 Klug, H. P. & Alexander, L. E. (1974). *X-ray Diffraction Procedures: For Polycrystalline and Amorphous Materials*. New York: John Wiley and Sons.
 Kriegner, D., Wintersberger, E. & Stangl, J. (2013). *J. Appl. Cryst.* **46**, 1162–1170.
 Langford, J. I. & Louër, D. (1996). *Rep. Prog. Phys.* **59**, 131.
 Larson, A. & Von Dreele, R. (2000). *GSAS*. Report LAUR 86–748. Los Alamos National Laboratory, New Mexico, USA.
 Leoni, M., Confente, T. & Scardi, P. (2006). *Z. Kristallogr. (Suppl.)*, **2006**, 249–254.
 Liermann, H.-P., Morgenroth, W., Ehnes, A., Berghäuser, A., Winkler, B., Franz, H. & Weckert, E. (2010). *J. Phys. Conf. Ser.* **215**, 012029.
 Louër, D. & Langford, J. I. (1988). *J. Appl. Cryst.* **21**, 430–437.
 Lutterotti, L., Matthies, S. & Wenk, H. R. (1999). *IUCr Commission on Powder Diffraction Newsletter*, No. 21, pp. 14–15.
 Materěj, Z., Kadlecová, A., Janeček, M., Materějová, L., Dopita, M. & Kužel, R. (2014). *Powder Diffr.* **29** (Suppl. S2), S35–S41.
 Materěj, Z., Kužel, R. & Nichtová, L. (2010). *Powder Diffr.* **25**, 125–131.
 McCusker, L. B., Von Dreele, R. B., Cox, D. E., Louër, D. & Scardi, P. (1999). *J. Appl. Cryst.* **32**, 36–50.
 Mittemeijer, E. J. & Scardi, P. (2004). *Diffraction Analysis of the Microstructure of Materials*, Springer Series in Materials Science. Berlin, Heidelberg: Springer-Verlag.
 Mittemeijer, E. J. & Welzel, U. (2013). *Modern Diffraction Methods*. Weinheim: Wiley VCH.
 National Institute of Standards & Technology (2010). *SRM 660b – Line Position and Line Shape Standard for Powder Diffraction*, https://www-s.nist.gov/srmors/view_detail.cfm?srm=660b.
 Paszkowicz, W. (2005). *Nucl. Instrum. Methods Phys. Res. Sect. A*, **551**, 162–177.
 Petříček, V., Dušek, M. & Palatinus, L. (2014). *Z. Kristallogr.* **229**, 345–352.
 Reiss, C. A. (2002). *IUCr Commission on Powder Diffraction Newsletter*, No. 27, pp. 21–23.
 Ribárik, G., Ungár, T. & Gubicza, J. (2001). *J. Appl. Cryst.* **34**, 669–676.
 Rietveld, H. M. (1969). *J. Appl. Cryst.* **2**, 65–71.
 Rodríguez-Carvajal, J. (1993). *Phys. B Condens. Matter*, **192**, 55–69.
 Scardi, P. & Leoni, M. (2002). *Acta Cryst.* **A58**, 190–200.
 Schmitt, B., Brönnimann, C., Eikenberry, E. F., Gozzo, F., Hörmann, C., Horisberger, R. & Patterson, B. (2003). *Nucl. Instrum. Methods Phys. Res. Sect. A*, **501**, 267–272.
 Slowik, J. & Zięba, A. (2001). *J. Appl. Cryst.* **34**, 458–464.
 Wright, V., Davidson, W., Melone, J., O’Shea, V., Smith, K., Donnohue, L., Lea, L., Robb, K., Nenonen, S. & Silpila, H. (2004). *Nuclear Science Symposium Conference Record*, Vol. 2, pp. 1336–1343. IEEE Conference Publications.
 Young, R. A. & Wiles, D. B. (1982). *J. Appl. Cryst.* **15**, 430–438.